# Quantitative skill of quasi-geostrophic forecasts of a baroclinically unstable Iceland-Faroe Front

Arthur J. Miller[1] and Pierre-Marie Poulain

SACLANT Undersea Research Centre, La Spezia, Italy

Allan R. Robinson, Hernan G. Arango, and Wayne G. Leslie

Division of Applied Sciences and Department of Earth and Planetary Sciences, Harvard University, Cambridge, Massachusetts

Alex Warn-Varnas

SACLANT Undersea Research Centre, La Spezia, Italy

**Abstract.** Using initialization and validation conditions from hydrographic surveys of the Iceland-Faroe Front in August 1993, shipboard quasi-geostrophic model forecasts executed in real time are evaluated for quantitative skill in terms of anomaly correlation coefficient and rms error. The prototype dynamical forecasts are synoptically initialized from two observed initial states and validated against observations obtained 3–4 days later. The forecasts correlate with the validating observations, yielding anomaly correlation coefficients of 0.75–0.80, which beat persistence-of-day-zero forecasts by 0.07–0.30, depending on the region of interest and the initial state. Thus this quasi-geostrophic model is able to forecast the rapidly evolving currents of this front with quantitative skill. The forecast fields of stream function are also used to diagnose the physical processes of the frontal current variations. Energetic diagnostics clearly reveal that the frontal current evolution is controlled by baroclinic instability processes. Baroclinic wave disturbances at middepth serve to transfer available gravitational energy to kinetic energy, which then is transferred through the water column, resulting in the observed (and modeled) rapid changes in the frontal current.

## 1. Introduction

One of the long-standing goals of physical oceanography has been to forecast oceanic mesoscale variability in a fashion similar to atmospheric forecasts of weather systems that are now routinely computed. Demonstrations of significant quantitative oceanic mesoscale forecasting skill are now beginning to be possible [*Ezer et al.*, 1992; *Fox et al.*, 1992, 1993; *Glenn and Robinson*, 1995; *Robinson et al.*, 1989], but better initialization and validation data as well as improvements in forecast model dynamics are desired in order to generate accurate verifiable forecasts.

In a previous study [*Miller et al.*, 1995] (hereinafter referred to as M95), we tuned a quasi-geostrophic (QG) forecasting model to reproduce an observed cold tongue intrusion (baroclinic instability) of the Iceland-Faroe Front (IFF), from observed hydrographic initial conditions in October 1992. The results of that discussion, however intriguing, were restricted by the qualitative (feature) validation strategy that was employed because the validation data set was extremely limited due to severe weather conditions during the cruise.

During a later cruise, in August 1993, that was carefully designed to obtain initialization, assimilation, and validation data, we were greeted with excellent weather conditions, so that we were able to independently test the tuned QG forecasting model in real time (or near real time) from two sets of initial conditions. Subsequent to the cruise, these forecasts were objectively validated against the observations in terms of anomaly correlation and rms error statistics, always referencing the skill score to persistence of day zero. This study is novel (and different from M95), in that we executed shipboard, real-time/near-real-time QG forecasts for which we are able to present a quantitative demonstration of forecasting skill for 3- to 4-day forecasts of the Iceland-Faroe frontal current, which is known to evolve radically over these short timescales and 10- to 50-km spatial scales [e.g., *Niiler et al.*, 1992].

After ascertaining that the model is able to successfully forecast variations of the frontal current, we turn to a diagnostic study of the energetic transfers in the simulations. We find that the occurrence of baroclinic wave disturbances, dynamically consistent with simple models of baroclinic instability, are the dominant mechanism of controlling energy transfers in the middle and upper water column. Thus the Iceland-Faroe frontal current can be viewed during this time interval as highly baroclinically unstable and forced by inflow from larger-scale current fields outside the sampling and modeling domain.

---

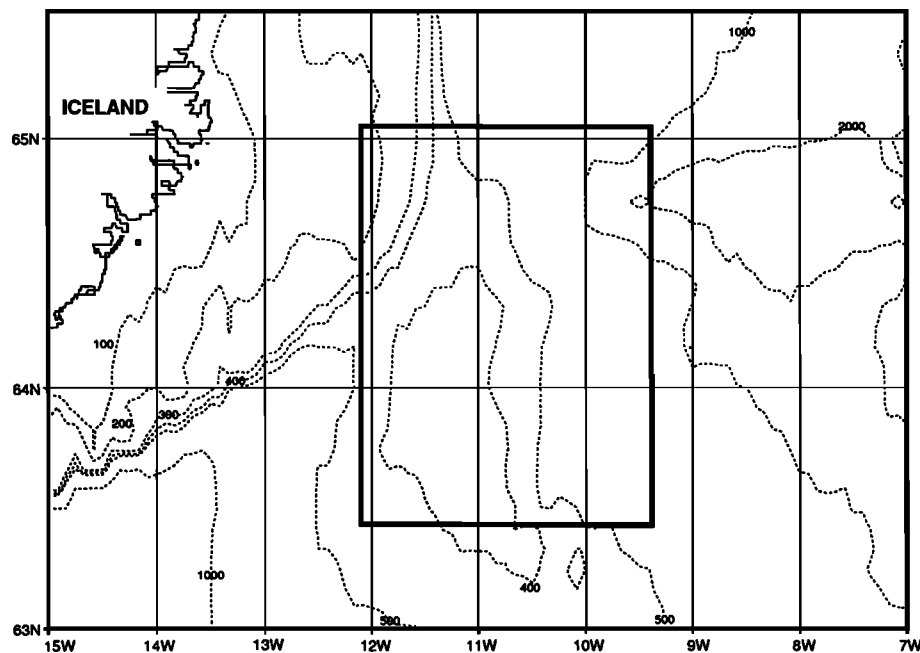[1]Now at Climate Research Division, Scripps Institution of Oceanography, La Jolla, California.

**Figure 1.** Bathymetry of the Iceland-Faroe frontal region (irregular contour intervals in meters). Rectangle indicates the quasi-geostrophic model forecasting domain.

## 2. Data Sets

### 2.1. Initialization and Validation Hydrographic Surveys

In August 1993, SACLANTCEN and Harvard University embarked on a joint expedition to the IFF (Figure 1) to conduct hydrographic surveys for real-time nowcasting and forecasting of frontal current variability, as well as to retrieve current meter moorings deployed during an October 1992 cruise and to conduct other physical process studies within that region [*Poulain*, 1993]. Because we were fortunate to enjoy good weather, we collected expendable bathythermograph (XBT), conductivity-temperature-depth (CTD), and expendable CTD (XCTD) data for three separate
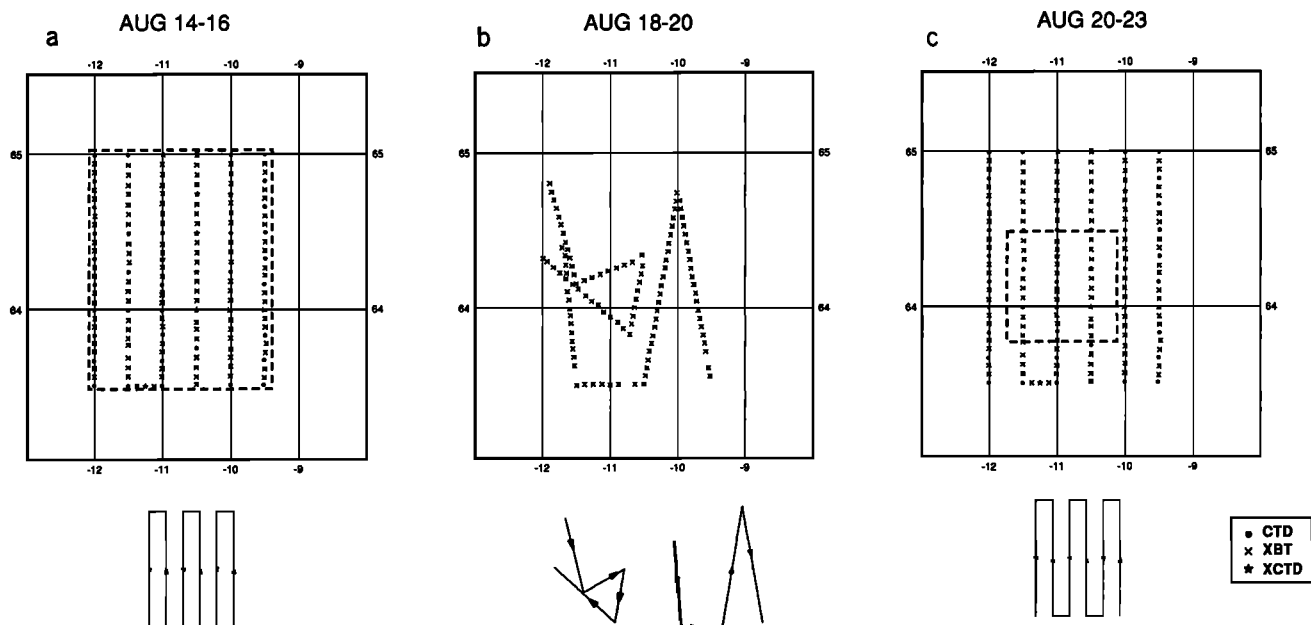


**Figure 2.** (a) Locations of the XBTs, XCTDs, and CTDs during the initialization survey. The survey was obtained from east to west from August 14 through August 16, 1993. (b) Same as Figure 2a but for the zigzag track, obtained from August 18 to 19, 1993. (c) Same as Figure 2a but for validation track, obtained from east to west from August 20–23, 1993. Also shown in Figure 2a is the model forecasting domain (dashed box), and in Figure 2c the subdomain (small box) of the energy budget analysis discussed in section 8.
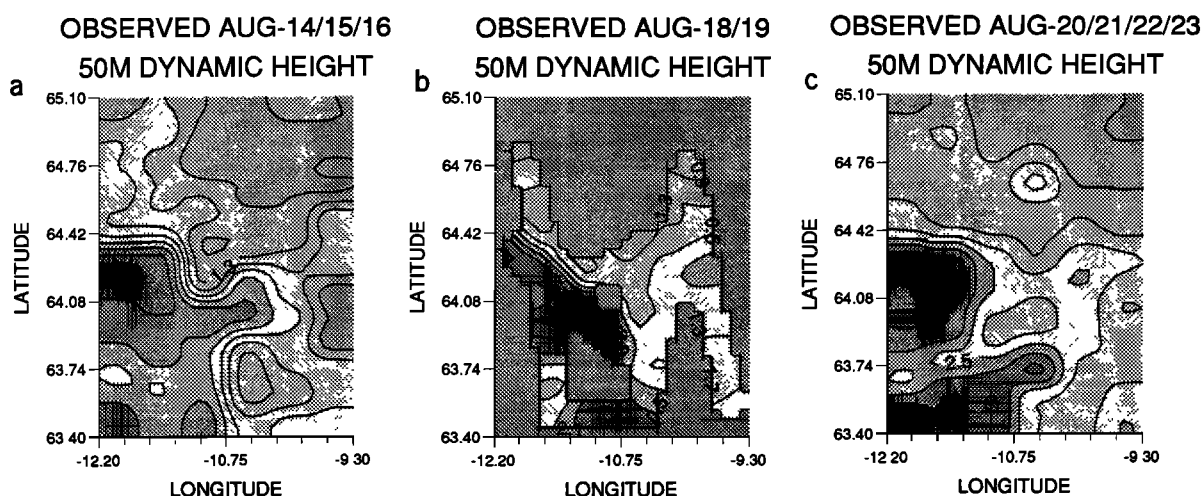
OBSERVED AUG-14/15/16 50M DYNAMIC HEIGHT    OBSERVED AUG-18/19 50M DYNAMIC HEIGHT    OBSERVED AUG-20/21/22/23 50M DYNAMIC HEIGHT

**Figure 3.** Objective analyses of dynamic height at 50 m relative to 400 m for the (a) initial, (b) zigzag, and (c) validating surveys. Contour interval (CI = 0.4); multiply plotted values by 5.92 to obtain dimensional dynamic height in centimeters.

surveys (Figures 2 and 3), hereinafter referred to as the initialization, zigzag, and validation surveys. Besides the hydrocasts, we deployed two sets of surface drifters [*Poulain*, 1993] in the core (August 18–19) of the IFF. One clear satellite image of sea surface temperature (SST) in the survey area was also available for August 22 (Plate 1).

The initialization survey spanned August 14–16 and included XBTs, XCTDs, and CTD data (Figure 2a) sampled at 24-km resolution in the east-west direction and approximately 7-km resolution in the north-south direction. The zigzag survey, from August 18 to 19, was specifically designed in real time to update (via assimilation) the IFF conditions and consisted solely of XBTs in and around the western central part of IFF (Figure 2b). For the purposes of assimilating the data of the zigzag survey into the model, it was further broken up into data from August 18 (the first zigzag) and from August 19 (the second zigzag). The validation survey, during August 20–23, charted the same track as the initialization survey, 7 days later, albeit slower paced because it included more CTDs among the hydrocasts.

Once the data were collected, they were visually preprocessed for obvious errors by inspecting the temperature and salinity as a function of depth to identify any obvious malfunctions of the XBTs or XCTDs. The XBT data were then supplemented with synthetic salinity data, which were derived from a temperature-salinity (T-S) water mass model constructed as follows. The first 15 CTDs were used to identify the distinctive local T-S relationships. From that group, three average T-S profiles were created, one each for the North Atlantic Water, for the East Icelandic Water, and for the frontal water. With those averages in hand, each XBT was identified as one of the three types, and the appropriate T-S relationship was used to match the observed temperatures with an associated salinity. Additionally, each hydrocast was extended, if necessary, via an exponential profile to 990-m depth (even if this exceeded the true depth of the water column). We note that after the cruise, some problems became evident, in that the water mass model resulted in a salinity offset (in the sense that the salinity front associated with only the XBT data was smeared northward in the sampling domain) and that several XCTDs were biased in

salinity as well. Since these salinity offsets are not crucial to the density distribution (i.e., temperature, along with the remaining good salinity observations, yielded an adequate density distribution), these salinity errors are left as is and are not accounted for in the following analysis of our real-time, shipboard forecasts.

For initial conditions, the QG model requires stream function, which we assume to be directly proportional to dynamic height. Since M95 found that a 400-m level of motion yielded the most realistic postcruise forecasts for the October 1992 data set, we also used a 400-m level of no motion to account for the unknown barotropic mode. Note that the M95 model applied to October rather than August conditions, so one might expect discrepancies in the level of no motion. On the other hand, we acquired surface drifter observations during the cruise that revealed peak speeds of approximately 76 cm/s (to the southeast) in the Iceland-Faroe frontal current. Although this speed is greater than the peak speeds of 58 cm/s derived from objectively analyzed initialization survey dynamic height at 50 m (relative to 400 m), these objective analyses may result in somewhat overly smoothed dynamic height gradients in the frontal current. Indeed, velocities predicted by the forecasts are higher than the initial condition velocities, peaking at 70 cm/s. This adjustment of the surface velocity field toward higher values during the simulation suggests that the dynamics sufficiently control the run, so that it is not overly dependent on the necessarily smooth initial state. The development of flow in the model level 4 during the forecast is also a check on whether it is truly a level of no motion. After about 3 days, the flows in level 4 tend to be in phase with those of level 3 (equivalent barotropic) with about half the amplitude. Thus the 400-m no motion assumption is not strictly valid but appears to be reasonably justified, though additional tests of the model using the present data set would be useful to determine a level of no motion at which flows remain weak during the forecast.

### 2.2. Synopsis of Iceland-Faroe Frontal Current Variability

Figure 3 shows the observed 50-m dynamic height field for the three surveys, with the zigzag survey only plotted where

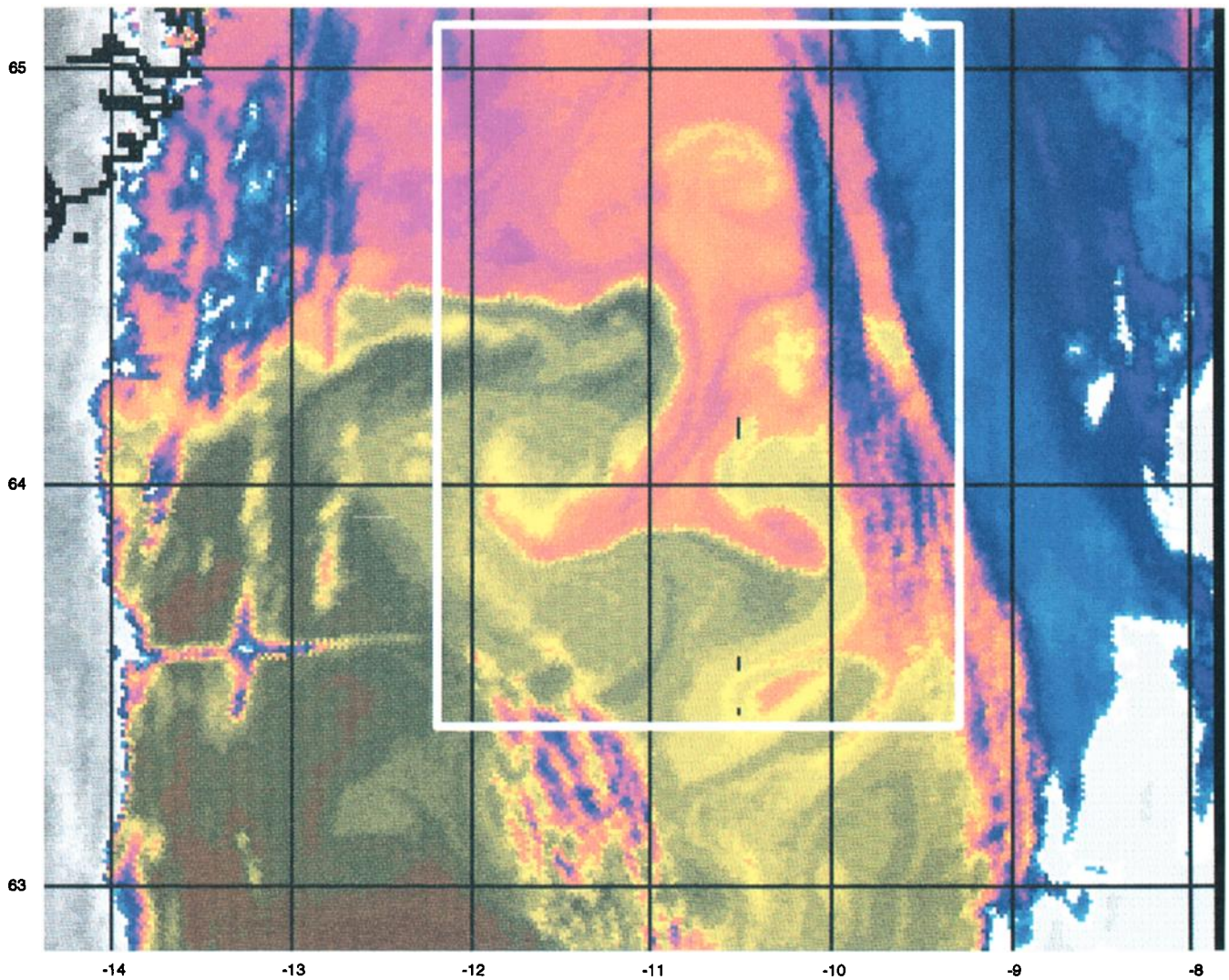## NOAA11 AVHRR CH4, 22-AUG-1993 14:31 GMT, GIN93 DOMAIN



**Plate 1.** Satellite infrared (channel 4 of advanced very high resolution radiometer (AVHRR)) image for August 22, 1993, 1431 UT. White and blue areas indicate clouds, pink areas cooler water, and green areas warmer water. The QG forecasting model domain is traced in the image. Part of the coast of Iceland is delineated in the upper left corner. The surface signature of the cold hammerhead intrusion is clearly evident.

the relative error is 20% or less to provide a mask of the survey. One observes that the frontal current initially had a steplike kink in the flow, which splits downstream in the eastern domain into a northeastward and southward branch. During the zigzag survey the frontal current had apparently changed significantly, by losing its kink and orienting itself in a southeastward direction. During the final survey, the frontal structure had altered itself once again, now exhibiting a strong eastward flow in the western domain, a southwestward flow in the central/southwestern domain, and an eastward flow across the central/southern domain. It is important to be aware that the location of the inflow of the frontal current into the model domain was, fortunately, nearly stationary throughout this time interval. Thus our (a priori) assumption of holding the inflow boundary condition fixed throughout the forecasts is consistent with the (a posteriori) observed inflow condition.

The single satellite image of SST for August 22 (Plate 1) shows that a large-scale hammerhead cold intrusion (or 'deep-sock meander' in Gulf Stream terminology) was present at that time. Examining the objective analyses of 10-m temperature (Figure 4), it is noteworthy that one cannot easily deduce by inspecting the hydrographic survey alone that a hammerhead intrusion is occurring. However, even though the surface signature of the hammerhead intrusion is not necessarily indicative of subsurface or midwater-column conditions, the hydrographic data are consistent with the satellite image. Thus the satellite image, combined with the temperature objective analyses and surface drifter tracks (Figure 4), furnishes us with a phenomenological description of what occurred during the latter part of the cruise.

The surface drifter observations corroborate the southeastward shift of the orientation of the Iceland-Faroe frontal current from the initial to the zigzag survey, the interpreta-
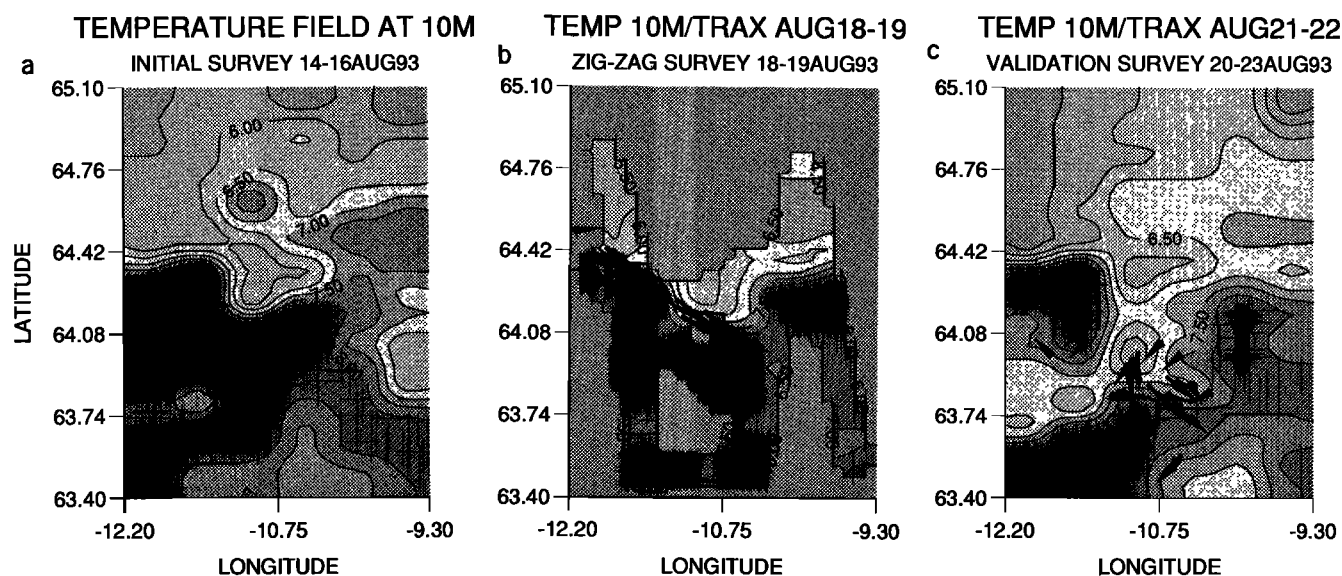
**Figure 4.** Objective analyses of temperature at 10-m depth for the (a) initial, (b) zigzag, and (c) validating surveys. Contour interval is 0.5°C. Twelve-hour surface drifter displacements are indicated by arrows in Figure 4b for August 18 and 19 and in Figure 4c for August 21 and 22.

tion of which must be treated cautiously due to possible spatial aliasing of the zigzag survey. The drifters for August 18 and 19 (Figure 4b) clearly show a southeastward flow at the surface and suggest that the zigzag survey did not spatially alias the frontal structure. From the steplike frontal current orientation on August 14–16, the front angled itself southeastward by August 18, after which the hammerhead grew rapidly to its final observed state on August 22. Note that shape of this cold hammerhead intrusion differs from the cuspate cold tongue intrusion observed and modeled by M95 (their Figure 5b), although both grow over similarly short timescales.

Finally, it is interesting to point out that the signature of the cold intrusion in the dynamic height field is not as clear as in the temperature field. The dynamic height field (Figure 3c) shows that the frontal current encircles the western and southern part of the hammerhead and then heads southward, while the satellite image (Plate 1) gives the impression that the current wraps around the intrusion with strong northward flow on the eastern flanks of the hammerhead. However, the dynamic height survey was gathered over a 3.5-day interval, so we cannot state with certainty that the northward flow on the eastern side of the cold intrusion is weak. The drifters (section 7) indicate a broad southwestward flow along the western side of the cold intrusion on August 21 followed by an eastward translation along the southern extremity of the hammerhead on August 22. The drifters do not enter the region around the eastern flanks of the hammerhead, further suggesting only weak geostrophic flow there.

## 3. ShipBoard Real-Time Forecasting Model

M95 studied the forecasting capability of the Harvard Open Ocean Quasigeostophic Model [Miller et al., 1981; Robinson and Walstad, 1987] to reproduce an observed cold tongue intrusion of the Iceland-Faroe frontal current during October 1992. This model was subsequently used in the real-time and near-real-time forecasts carried out at sea during the August 1993 cruise; primitive equation model forecasts were concurrently executed and are discussed in a separate publication (A. R. Robinson et al., Real time operational forecasting on shipboard of the Iceland-Faeroe Frontal variability, submitted to *Bulletin of the American Meteorological Society*, 1995; hereinafter referred to as submitted manuscript). The QG model integrates the potential vorticity equation, written in nondimensional form as

$$\frac{\partial q}{\partial t} + \alpha J(\psi, q) + \beta \frac{\partial \psi}{\partial x} = F_S \tag{1}$$

where

$$q = \nabla_h^2 \psi + \Gamma^2 \left( \sigma \frac{\partial \psi}{\partial z} \right)_z \tag{2}$$

where $\psi$ is the QG stream function, $J(\ ,\ )$ is the Jacobian operator, and $\nabla_h^2$ is the horizontal Laplacian operator. With characteristic scales, $L = 15000$ m, $T = 50000$ s, and $U = 0.3$ m/s, the nondimensional parameters become $\alpha = TU/L = 1.0$ and $\beta = \beta_o TD = 0.0078$. Horizontal eddy diffusivity $F_S$ in the QG equation is modeled by applying a very weak, fourth-order Shapiro filter, twice each time step. The parameters $\Gamma^2$ and $\sigma$ describe the stratification of the region and are chosen so that vertical modes of the discretized model correspond with vertical modes computed from observed climatological stratification in the area. The model is discretized in five layers (centered at 50-, 150-, 250-, 400-, and 600-m depth), with 5-km resolution in both horizontal directions on a 27 by 37 grid point domain centered on (64.25°N, 10.75°W). A flat bottom was used since M95 found that little difference results when including a smoothed version of the Iceland-Faroe ridge over the 5-day time interval of their forecasting experiment; the primitive equation model forecasts (A. R. Robinson et al., submitted manuscript, 1995) include a proper treatment of topography.

**Table 1.** Prototype Shipboard QG Forecasts

| | Initial Dates | Initialization Type | Completion Date |
|---|---|---|---|
| Case 1 | Aug.14–16 | synoptic | Aug.19 |
| Case 2 | Aug.14–16 | assimilated/expanding domain | Aug.20 |
| Case 3 | Aug. 18 | assimilated with case 2 | Aug.20 |
| Case 4 | Aug. 19 | assimilated with case 3 | Aug.20 |

Over longer timescales, topography cannot be neglected, since it is essential in establishing mean conditions in the IFF.

Our fundamental assumption is that intrinsic ocean dynamics are responsible for the synoptic-scale variability of the IFF. Since wind stress and/or surface heat flux variations typically have much larger spatial scales than those of the IFF, we applied no external atmospheric forcing to the system. The only forcing is via inflow/outflow conditions implied by holding the boundary conditions fixed at their initial values (persistent boundary conditions) and by specifying the initial conditions of the interior stream function. If the location of the frontal current inflow changes appreciably during the time interval of the forecast, this assumption of persistent boundary conditions breaks down, and we would only expect the forecast to have potential merit in the interior of the domain (far from the inlet condition). Based on the best results of M95, we invoked parameters for the assumed isotropic autocorrelation function $R(r) = 1 - (r/a)^2 \exp[-(r/b)^2]$ of the objective analysis scheme of $(a, b, \text{err}) = (10 \text{ km}, 60 \text{ km}, 0.1) = $ (zero crossing, exponential decay, error), which controls the smoothness and precision of the initial conditions and verification analyses [*Carter and Robinson*, 1987]. The objective analyses are done separately for each model layer; examples of these objective analyses are shown in several of the figures (e.g., Figure 3).

## 4. Forecast Initialization

The three hydrographic surveys present us with two separate synoptic realizations (August 14–16 and 18–19) for which forecasts can be validated by the surveys 3 days (August 18–19) and 4 days (August 21–23) later, respectively. Forecasts from the August 14–16 initialization can also be validated 7 days later. Since M95 showed that poorer forecasts resulted when attempting to account for nonsynoptic data using a simple assimilation scheme, we considered the synoptically initialized forecasts to be prototypical; additional assimilated initial states, discussed subsequently, are referred to as experimental.

In case 1, the August 14–16 survey was treated synoptically, and forecasts were run out to 8 days. For case 2, the August 14–16 survey was treated in an assimilative fashion by breaking up the full domain into three subdomains corresponding to the first two legs, the second two legs, and the third two legs of the total survey. The objectively analyzed data from August 14 (eastern third of the survey) were used as initial conditions to forecast to August 15, with persistent boundary conditions in a domain one third as wide as that shown in Figure 3. Then, in a domain two thirds the size of that shown in Figure 4, the objective analysis from August 14–15 (eastern two thirds of survey) was replaced by

the interior gridded forecast data for August 15 in the eastern third of the domain, resulting in the initial state for August 15. This field was stepped forward 1 day in time (with persistent boundary conditions from the objective analysis of August 14–15) to day 16. Likewise, the objective analysis from August 14–16 (entire survey) was replaced by the interior gridded forecast data for August 16 in the eastern two thirds of the full domain to produce the initial state for August 16. The case 2 forecast was then run for 8 days from this assimilated initial condition with persistent boundary conditions.

Since the zigzag survey of August 18–19 had too few data to completely reinitialize the entire model domain, we assimilated the data into the forecast by optimal interpolation as follows. A local objective analysis of the data is first performed at the assimilation time step. Then the objectively analyzed observations are assimilated by blending them with the gridded forecast at the same time step. The weights of the blending are calculated as a function of the error field, $\varepsilon(x, y)$, of the objective analysis, such that $\psi_{assim} = (1 - \varepsilon)\psi_{OA} + \varepsilon\psi_{fc}$. This was done at only one time step, after which the model was reinitialized with a forward step. Thus at a grid point that coincides with a CTD measurement, for example, the weighting is 0.9 for the observation and 0.1 (the assumed observational error level) for the model forecast. Away from direct measurements, the weighting more heavily favors the model forecast for that day. The forecast of case 2 for August 18 was thus assimilated with the data acquired on August 18 (first zigzag) such that case 3 is the 8-day forecast from this assimilated initial state on August 18. From the forecast for August 19 of case 3 (1-day forecast), we then blended the data acquired on August 19 to reinitialize the model for that day. Case 4 is the 8-day forecast from this initial state on August 19.

Table 1 lists the features of these four prototypical shipboard QG forecasts, along with their completion date. Table 2 lists the additional shipboard QG forecasts that were either done incorrectly (case 1a and 1b) or were a test (case 5). For cases 1a and 2a, which were completed in real time on August 17, a large number of hydrocasts (26 out of 154) were inadvertently deleted from the initial dynamic height fields. When this error was discovered, these cases were subsequently rerun at sea with all the initial data (cases 1 and 2) and completed in near real time on August 19. Cases 3 and 4 were completed in real time on August 20. In case 5 the hydrographic survey was subsampled at 27-km north-south resolution to determine how a much more poorly resolved survey would fare relative to the prototype case 1.

## 5. Validation Strategies

Given that we have unprecedentedly complete initial conditions and validating conditions, we adopt standard

**Table 2.** Additional Shipboard QG Forecasts

| | Initial Dates | Initialization Type | Completion Date |
|---|---|---|---|
| Case 1a | Aug. 14–16 | case 1 with 26 missed hydrocasts | Aug.17 |
| Case 2a | Aug. 14–16 | case 2 with 26 missed hydrocasts | Aug.17 |
| Case 5 | Aug. 18 | case 1 subsampled at 50-km resolution | Aug.19 |

statistical validation measures, namely, anomaly correlation coefficient (ACC) and rms error, viz.,

$$ACC \equiv \frac{\langle \psi_p' \psi_o' \rangle}{(\langle \psi_p'^2 \rangle \langle \psi_o'^2 \rangle)^{1/2}} \quad (3)$$

and

$$rmse \equiv \langle (\psi_p - \psi_o)^2 \rangle^{1/2} \quad (4)$$

where $\psi_p$ is the predicted stream function, $\psi_o$ the observed stream function (i.e., dynamic height scaled to stream function as done for the initial conditions), the primes denote removal of the areal mean, and the angle brackets denote averaging over the specified horizontal area. We remark that $\psi_p$ will apply either to the dynamical prediction or to using persistence of day zero as the predictor. Our measures of quantitative skill here will always be judged with respect to persistence of the initial (day zero) observations.

When computing pattern correlations between fields that have a significant trend in space (i.e., around the front), one expects a relatively high value of the correlation no matter how poorly the actual fields may agree. In other words, since the front always bounds cold water to the north (low dynamic height) and warm water to the south (high dynamic height), it would be preferential to remove the mean climatology before computing correlations to account for this trend in space. But since we have no accurate mean climatology that properly resolves the front to the precision of our survey, we will simply bear in mind that the correlations will be artificially high, and we will only emphasize the increases in correlation that a dynamical forecast produces relative to persistence of day zero.

In meteorology, where there is plenty of validating data on each day of a forecast, it is typical to plot the correlation decay or error growth as a function of time as the forecast becomes increasingly more erroneous [e.g., *Holloway and West*, 1984]. Moreover, since there are multitudes of initial conditions, one can ascribe some measure of statistical confidence to the plotted correlation decay by ensemble averaging over many independent initial states. In our case, we have neither validating information on each day of the forecast nor a multitude of initial conditions. We can thus ascribe no significance levels to our estimates of quantitative skill. Furthermore, the two initial states (August 16–18 and 18–19) are not uncorrelated. Thus the results must be viewed as suggestive but not conclusive evidence of true forecast skill in the model.

In lieu of plotting correlation decay as a function of time between forecast and observations (which in our case would be a plot with only two points, ACC = 1.0 at time zero and ACC < 1 at day $N$), we plot the correlation between the forecast for each day with the observations on the single day of validation [cf. *Glenn and Robinson*, 1995]. This view of the relation between forecast and observations allows us to identify potential inadequacies in the time evolution of model dynamics in the sense that, for example, a day ($N$ + 2) forecast might be a superior predictor of day ($N$) observations, indicating that the model eddy features mature too slowly in time. If the correlation between the observations on day $N$ is maximum for the forecast on day $N$, we have the pleasing result that the model fields are evolving consistently in time vis-a-vis the observed fields. The plots also afford an indication of how rapidly the fields decorrelate in time.

Since we treat a 3-day survey (August 14–16) as synoptic in case 1, and use a 3.5-day survey (August 20–23) as a synoptic validation for cases 3 and 4, we must decide on a way to ascribe a single date to the two surveys. Since the vast majority of synoptic activity is associated with frontal current evolution in the eastern-central part of the domain, and since the first zigzag survey on August 18 keenly captured the frontal structure in that area, we choose the days for which the survey passed through that region as appropriate. Thus, since the initial survey captured the kink in the frontal current on August 15, we ascribe that date to the synoptically treated initialization survey. (A 3-day forecast then applies to validating with the first zigzag survey on August 18.) Also, since the validating survey measured that same region on August 22, we ascribe it to have that date for purposes of validating cases 3 and 4. (A 4-day forecast thus pertains to reinitializing with the first zigzag forecasting the validation survey.)

Only the top three layers of the five-layer QG model are tested for skill for the following reasons. Since the model has an assumed level of no motion at 400-m depth (layer 4), the model forecast for layer 4 can only get worse than persistence of day 0 (no flow), so this layer is not discussed in any of the following comparisons. Similarly, layer 5 is centered at 600-m depth and is thus deeper than the actual water column in some parts of the model domain. In that case, this layer has observations that are synthetic (exponential extensions of overlying hydrocasts), so we do not study this layer's skill either. The physical process justification for concentrating attention on the upper portion of the water column was drawn up by M95, viz., that the modeled baroclinic instability tended to be surface intensified over the several-day timescale of the growth of a cold tongue intrusion. Since the modeled response tends to be equivalent barotropic, in the sense that stream function in the top three layers is spatially in phase but with weaker amplitudes at depth relative to the surface, the figures discussed below generally only show the top layer stream function.

We last discuss how the area over which the ACC and rmse is computed. Ideally, one would like to compute skill scores over regions where both good initial data and good verification data exist. In our case, there are data available over the entire domain for both the initial and validating hydrocast tracks, so one can happily test for skill over the whole domain for the case 1 forecast at 7 days. But for the zigzag survey, which serves as a verification for cases 1 and 2 and as an reinitialization (via assimilation) for case 3, only a portion of the region is surveyed. We must therefore define subregions of the domain, and to do so, we use the error field of the objective analysis for the zigzag surveys. The first zigzag is particularly crucial because it was specifically designed (at sea) to sample in and around the frontal current that is indeed where maximum changes occur and where the dynamics are most interesting and most challenging to predict.

Figure 5 shows the averaging areas for the skill scores. Region 1 is defined to be the entire domain. Region 2 includes only the area of the objective analysis of the entire 2-day zigzag survey where the error is 20% or less. Region 3 is the rectangular subdomain from 63.7°N–64.5°N and 12.2°W–10.0°W, overlapping mainly the first zigzag taken on August 18 (plus part of the first leg of the zigzag on August 19). Region 4 is the intersection of regions 2 and 3, which
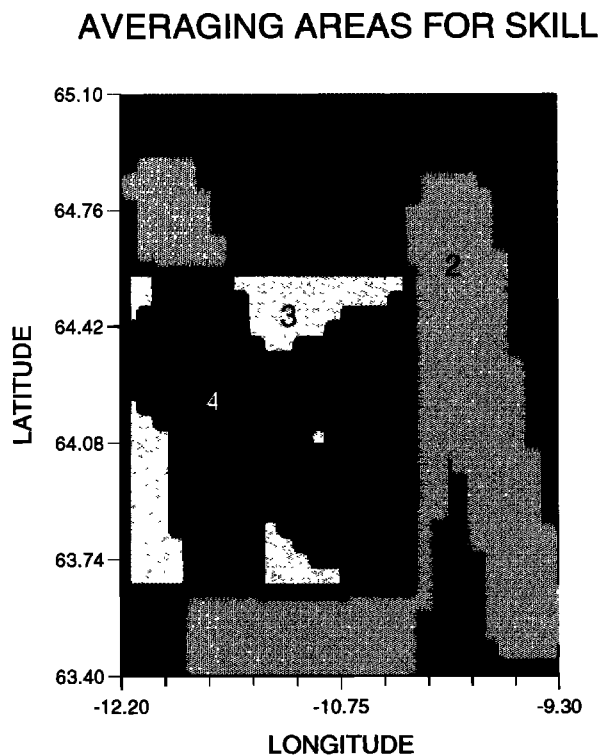
## AVERAGING AREAS FOR SKILL



**Figure 5.** Areas defined in the text over which averages are computed for skill scores. Region 1 is the entire domain, region 2 is the entire zigzag survey, region 3 is the rectangular area encompassing the evolving frontal current, and region 4 is the dark area, the intersection of the zigzag area and region 3.

includes only the region where the error of the objective analysis of the zigzag survey is 20% or less inside the rectangular box.

Note that other measures of quantitative skill could be employed such as mean axis error of the frontal current [e.g., *Ezer et al.*, 1992; *Fox et al.*, 1992, 1993; *Glenn and*

*Robinson*, 1995], denumeration of eddy events that occur during the forecast and validation [e.g., *Robinson et al.*, 1989], or by examining phase error in space as well as in time. We have chosen the rather standard skill measures of rmse and ACC for simplicity and directness.

## 6. Skill Scores

We now present the results of an objective and quantitative skill assessment for the QG forecasts that were executed during the August 1993 cruise to the IFF. We concentrate on the prototypical forecasts listed in Table 1.

### 6.1. August 14–16 Initial Conditions

**6.1.1. Three-Day Forecasts.** Figure 6 shows the layer 1 model initial conditions and the forecast for day 3 (August 18) for case 1, which may be compared directly with Figures 3a and 3b. The model forecast visually correlates with the observations on August 18–19, in that the frontal current loses its kink and shifts to a southeastward direction. The quantitative assessment of skill confirms this visual correspondence in both regions 2 and 4. Figure 7 shows the anomaly correlation coefficient between each day of the forecast and the observations on August 18–19 for each of the top three layers of the QG model in region 2 (the entire zigzag survey). The forecast of "persistence of day zero" for the observed initial conditions is indicated by the dashed line. The figure shows that the model forecast for day 18 correlates better (roughly a 0.07 increase, from 0.73 to 0.80 ACC) with the observations for August 18–19 than does persistence. The forecast field thus is able to explain an additional 10% of the stream function variance relative to persistence. Figure 7 also demonstrates that the modeled development of the southeastward flowing jet is contemporaneous with the observations, because the forecast skill peaks for forecasting August 18. The case 1 forecast also exhibits an eddy-shedding event, in that the perturbation near (64°N, 10°W) pinches off to form the warm eddy seen in Figure 6 to the northeast of its original position. Although a warm-eddylike structure is indeed seen in the observations
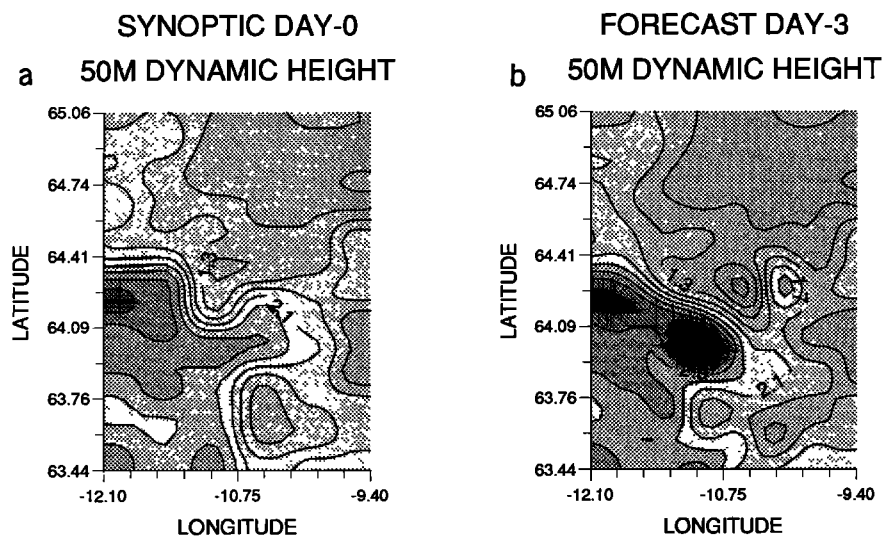


**Figure 6.** Case 1 (a) initial condition and (b) day 3 forecast of 50-m nondimensional stream function (CI = 0.4; multiply by 4500 to redimensionalize to m²/s). Compare directly with Figures 3a and 3b.

for the zigzag survey, the predicted eddy is displaced in space from that observed, so there is no quantitative skill in forecasting its location, even though its genesis is usefully forecast.

We next focus in on the variability in and around the frontal current by inspecting the skill scores for case 1 in region 4. These are shown in Figure 8 (ACC) and Figure 9 (rmse). The observations now more precisely correspond to August 18, since the first zigzag encompassed the IFF at that time. The ACC between model forecast day 3 (August 18) again is the maximum value and represents an increase over persistence of more than 0.11 for each of the three layers. A small decrease ($\approx 10\%$) in the rmse also occurs for day 18 of the case 1 forecast in the top two layers. Taken together, these skill scores indicate that the model is capturing the key



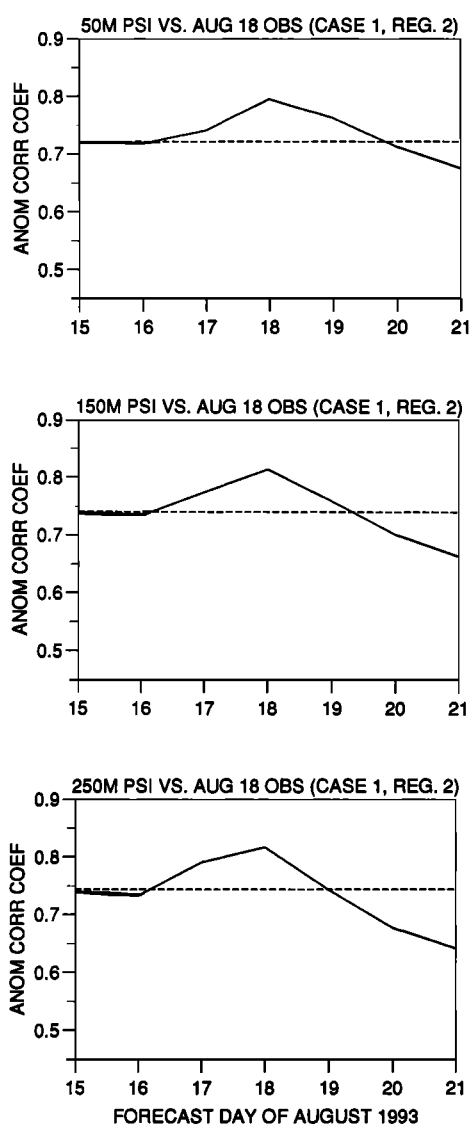Figure 8. Same as Figure 7, but for region 4.



Figure 7. Anomaly correlation coefficient for region 2 computed between each day of the case 1 forecast of dynamic height and the observations on August 18–19, plotted as solid line. Dashed line is the correlation between initial observations on August 14–16 and verifying observations on August 18–19. Plotted from top to bottom are results for layer 1 (50 m), layer 2 (150 m), and layer 3 (250 m).
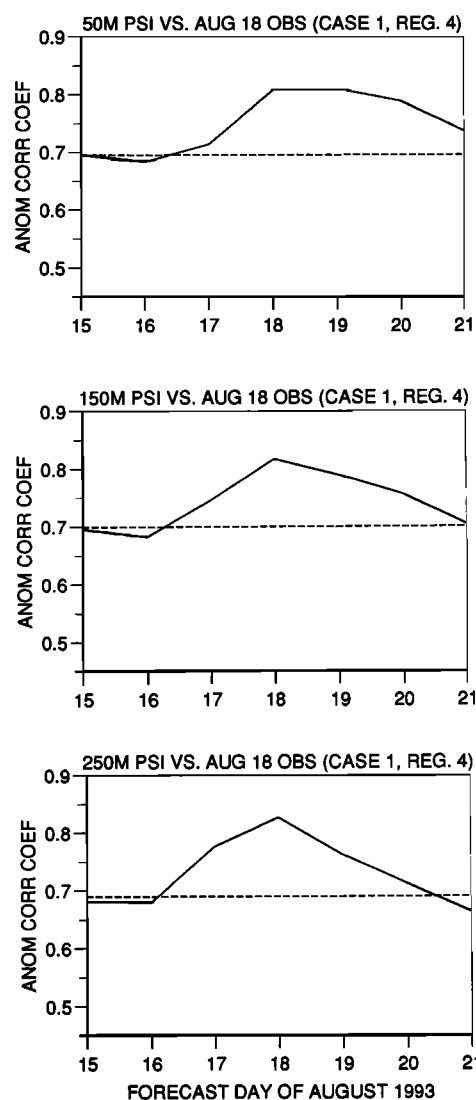
process that leads to the loss of the kink in the initial frontal current and its reorientation in a southeastward direction.

The skill scores for case 2 are listed in Table 3 and indicate no skill is present in the forecast. It is evident when perusing the evolution of the frontal current in this forecast that the assimilation procedure causes the model to retain the kink in the frontal current and to rapidly shed a large eddy into the south-central domain. Consistent with the results of M95, the synoptic initial conditions fare better than the assimilated initial state. Cases 1a and 2a, which failed to include all the initial hydrocast data, also had little or no skill over persistence of day zero. On the other hand, case 5, which we intentionally subsampled at 27-km north-south resolution, showed slightly more skill in both ACC and rmse (Table 1) than case 1. It thus appears that this particular initial state allowed such subsampling to be as efficient as a quadrupled sampling rate in the north-south direction and suggests that roughly 25-km sampling is sufficient for initializing forecasts in the region of the IFF. The lower rmse for case 5 appears to be a consequence of the smoother initial state generating less small-scale variability by day 3 of the forecast.
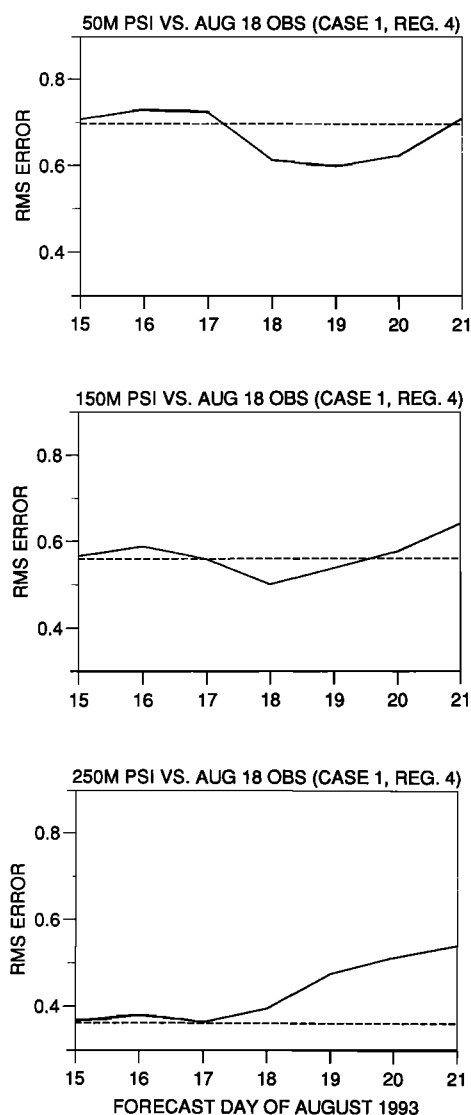
MILLER ET AL.: QUANTITATIVE FORECAST SKILL

**Figure 9.** Same as Figure 8, but for rms error.

**6.1.2. Seven-Day Forecasts.** Forecasting out to 7 days from the August 14–16 initial conditions yielded no quantitative skill in QG forecasting for either case 1 or case 2. This is the case when validating for the entire domain (region 1) or for the subdomain around the variable front (region 3). Forecasting this type of explosive instability, which developed over a 3-day timescale beginning August 18, from August 14–16 initial conditions, is evidently beyond the capability of this QG model. However, it should be noted that qualitatively useful information may yet be obtained from forecasts with no quantitative skill based on our chosen measures, e.g., the occurrence of eddy events or shifts in the frontal current direction. This aspect of these forecasts will not be pursued in this paper.

**6.2. August 18–19 Initial Conditions**

The initial conditions for case 3 and its 4-day forecast for August 22 are shown in Figure 10, which may be directly compared with Figures 3b and 3c. The visual correspondence between the observed and forecast dynamic height is impressive. From the southeastward oriented frontal flow in

the initial conditions, the model reproduced the western flanks of the cold hammerhead intrusion quite well. The warm eddy that the model produced to the south of the hammerhead intrusion would likely have merged with the evolving conditions at the southern boundary of the model domain had the boundary conditions been allowed to mimic the observed changes seen in Figure 3.

The raw skill scores for the ACC are impressive for case 3, as seen in Figure 11 and Table 4. The improvement over persistence of day zero of the observations alone is roughly 0.30 for each of the top three layers and has its maxima on day 4 (August 22), as one would hope. The rmse scores, however, show no skill over persistence and indicate that the model is overly energetic at this time. Since case 3 is initialized using data from August 18 (the first zigzag) melded with the forecast from case 2 for August 18, the persistence forecast for the observations alone (dashed line in Figure 11) is inferior to the persistence forecast for the assimilated initial conditions. However, referencing the model forecasts to persistence of these initial conditions still yields improvements to the ACC that are greater than 0.20 (and rmse scores that are commensurately poorer).

The three-day forecast for case 4 also exhibits increased ACC over persistence of the initial observations for both regions 2 and 4 (Table 4). However, relative to persistence of the assimilated initial state, it has essentially no skill for region 2. For region 4, relative to the assimilated initial conditions, the ACC increase drops to roughly 0.15, with similar rmse changes as for persistence of the initial data alone. However, the spatial structure of the forecast fields of stream function are not so visually similar to the observed as for case 3. North of 64°N, case 4 is similar to case 3, but south of that latitude, case 4 develops a strong southeastward oriented current rather than the eastward flowing current seen in the observations and along the north face of the eddy in case 3. Thus, although this forecast has skill in the region of the IFF, it has less skill than case 4, apparently due to the elementary assimilation scheme.

All in all, this demonstration of quantitative skill for two different initial conditions, for forecasts out to 3 or 4 days is an important validation of this QG model's ability to capture the essential dynamics of the Iceland-Faroe frontal current,

**Table 3.** Forecast Skill Versus Persistence of Day Zero: QG Forecast for August 18–19

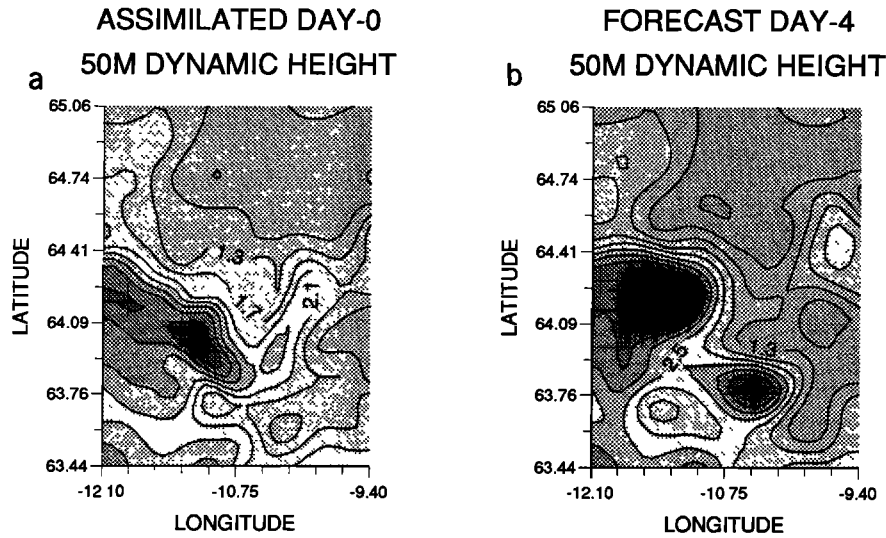| | Dynamic Height in Layers 1, 2, and 3 | | | |
|---|---|---|---|---|
| | Region 2 | | Region 4 | |
| | ACC Change | rmse Change, % | ACC Change | rmse Change, % |
| Case 1 | +0.073 | −7 | +0.111 | −12 |
| | +0.073 | −6 | +0.118 | −11 |
| | +0.073 | +11 | +0.136 | +9 |
| Case 2 | −0.037 | +12 | +0.013 | +7 |
| | −0.066 | +26 | −0.023 | +21 |
| | −0.073 | +64 | −0.041 | +58 |
| Case 1a | +0.018 | +7 | +0.077 | +0.6 |
| | +0.017 | +11 | +0.087 | +3 |
| | +0.008 | +35 | +0.095 | +29 |
| Case 5 | +0.077 | −17 | +0.139 | −29 |
| | +0.061 | −15 | +0.140 | −29 |
| | +0.041 | −2 | +0.150 | −22 |

**Figure 10.** Case 3 (a) initial condition and (b) day 4 forecast of 50-m nondimensional stream function (CI = 0.4; multiply by 4500 to redimensionalize to $m^2/s$). Compare directly with Figure 3b and 3c.

particularly when considering the qualitative skill documented by M95.

## 7. Corroboration With Surface Drifter Displacements

A peculiar feature of the observations and the model forecasts is that before the hammerhead intrusion formed, the frontal current oriented itself in an southeastward direction. Had we sampled the IFF only twice, on August 14–16 and on August 20–23, one might have drawn the conclusion that the initial kink in the frontal current simply grew into the hammerhead intrusion. That this did not occur is shown by both the skillful model forecast of case 1, which predicts the southeastward flowing current on August 18–19, and by the zigzag survey and surface drifter measurements. Figure 12 shows 12-hour drifter displacements for August 18–21 superposed on the initial conditions (August 18) and forecast (August 19–21) surface layer (50 m) stream function from case 3. Besides following the core of the southeastward oriented frontal current on August 18–19, the model successfully predicts the southward displacements that occurred on August 20 on the waxing westward face of the hammerhead event. The weak southwestward displacements on August 21 are not predicted by the model, although south of the southward extremity of the hammerhead intrusion there is a region of very weak flow.

## 8. Physical Processes of Iceland-Faroe Frontal Current Meandering

Presented with the two initial states and the 3- to 4-day skillful forecasts from each state, we next attempt to break down the dynamics of the model to elucidate the physical processes that lead to the rapid variations in frontal structure. Case 1 (for the interval August 15–18) and case 3 (for the interval August 18–22) are selected, since they both exhibited skill superior to persistence of day zero and because the modeled variability of the Iceland-Faroe frontal current strongly resembles the observed dynamic height

variability. The variability of the frontal current in the western and central parts of the domain are of paramount interest, so we focus in on that region as a subdomain for the energy diagnostics (see Figure 2c and Plates 2 and 3). The first three forecast days of case 1 correspond to the energetics of August 16–18. After reinitialization on August 18, the energetics of case 3 are considered for the following 4 days, August 19–22.

Following M95, we adopt the analysis procedure devised by *Pinardi and Robinson* [1986] for diagnosing the energetics of time-dependent model QG fields. The quasi-geostrophic kinetic and available gravitational potential energy (KE and AGE, respectively) equations in nondimensionalized form are (see *Pinardi and Robinson* [1986] for full details)

$$\dot{K} = -\alpha \nabla \cdot (\mathbf{u}K) - \nabla \cdot (p\mathbf{k} \times \mathbf{u}_t + \alpha p\mathbf{u} \cdot \nabla(\mathbf{k} \times \mathbf{u})$$

$$- \beta y p\mathbf{u}) + (p\sigma\Gamma^2 p_{zt} + p\alpha\Gamma^2 \sigma\mathbf{u} \cdot \nabla p_z)_z + \delta_o w \quad (5a)$$

$$\dot{K} = \Delta F_K + (\Delta F'_\pi + \Delta F^\alpha_\pi + \Delta F^\beta_\pi) + (\delta f'_\pi + \delta f^\alpha_\pi) - b \quad (5b)$$

$$\dot{K} = \Delta F_K + \Delta F_\pi + \delta f_\pi - b \quad (5c)$$

$$\dot{A} = -\alpha \nabla \cdot (\mathbf{u}A) - \delta_o w \quad (6a)$$

$$\dot{A} = \Delta F_A + b \quad (6b)$$

where the variables in (5) and (6) have their usual physical oceanographic meanings and the symbols in (5b), (5c), and (6b) correspond to the terms in (5) and (6) for ease in subsequent referencing. The nondimensional parameters $\alpha$ and $\beta$ were defined previously, and $\Gamma^2 = f_o^2 D^2/N_o^2 H^2$ and $\sigma = N_o^2/N^2(z) = -N_o^2/g(\partial\bar{p}/\partial z)$.

The symbols representing the terms in (5) and (6) are $\Delta F_K$, the horizontal KE advective working rate; $\Delta F_\pi$, the horizontal pressure working rate, which is further broken up into three terms, $\Delta F'_\pi$, that due to acceleration of the geostrophic velocity, $\Delta F^\alpha_\pi$, that due to advection of the geostrophic velocity, and $\Delta F^\beta_\pi$, that due to Coriolis acceleration; $\delta f_\pi$, the vertical pressure working rate, which is further broken
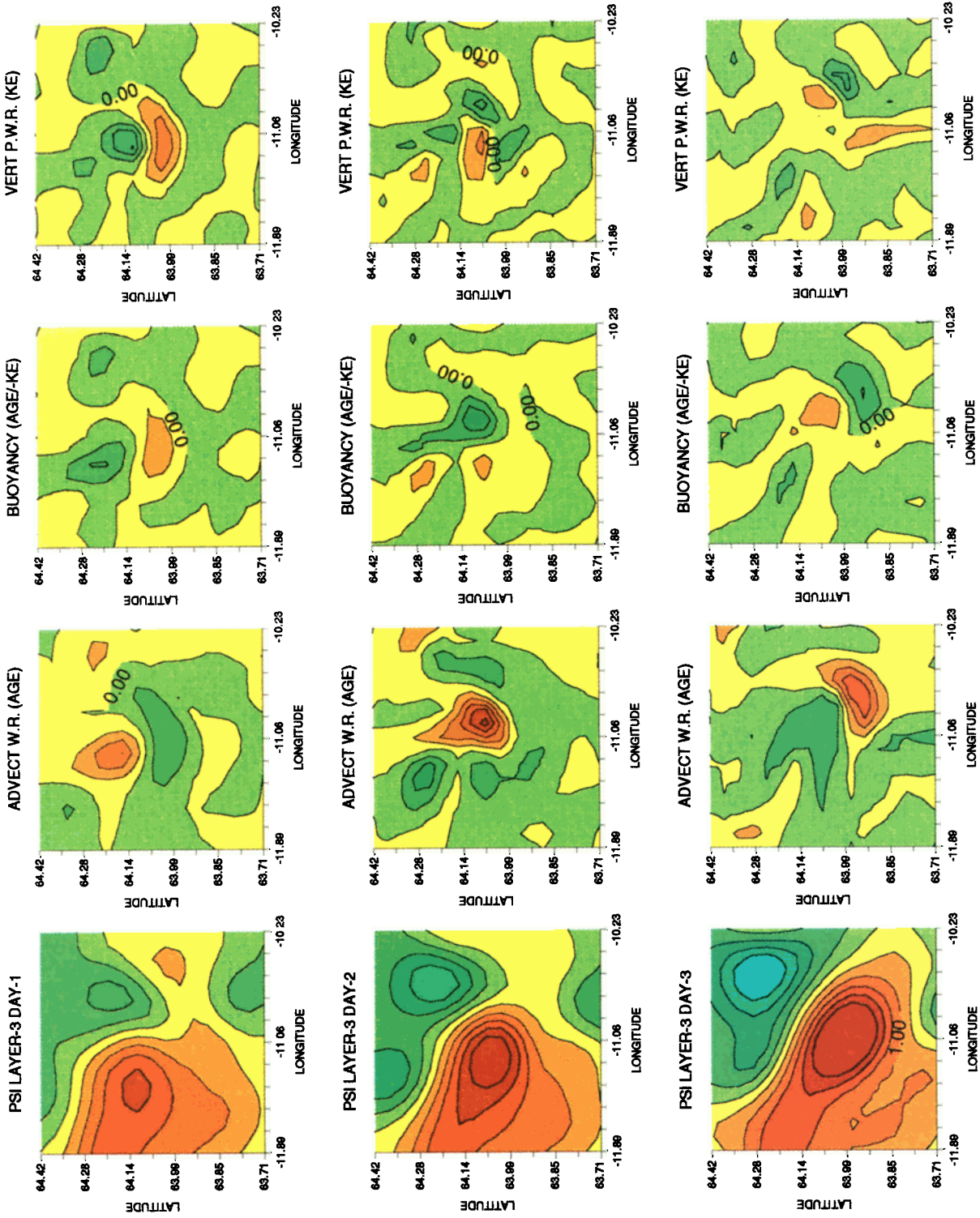
**Plate 2.**  Case 1 subdomain spatial fields for layer 3 (250 m) of $\psi_p$, $\Delta F_A$, $b$, and $\delta f_\pi$ for (top to bottom) day 1 through day 3 of the forecast from the AGE and KE equations (5b) and (6b). Stream function contour interval is 0.25 (scaling as in Figure 6) and 5.0 nondimensional units [following *Pinardi and Robinson*, 1986] for the other plots.
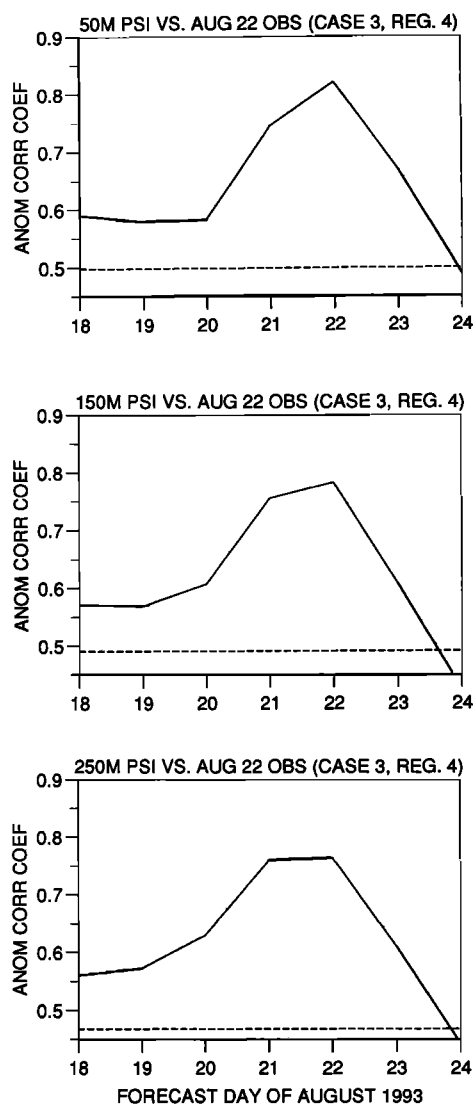
**Figure 11.** As in Figure 8 but for case 3. Note that the initial assimilation yields a superior prediction for persistence of day zero than do the pure observations.

up into two terms, $\delta f\,'_\pi$, the vertical pressure energy flux divergence due to time changes in density, and $\delta f\,^\alpha_\pi$, the vertical pressure energy flux divergence due to horizontal advection of density; $b$, the buoyancy working rate; and $\Delta F_A$, the horizontal AGE advective working rate.

As benchmarks, *Pinardi and Robinson* [1986] examined a set of simplified models (viz., a baroclinic Rossby wave, the Eady baroclinic instability problem, a case of barotropic instability, and an OPTIMA-V eddy merger event) in order to build a catalogue of what time-dependent balances of terms should be expected when one or another physical situation is manifest in the simulation. Other published accounts of QG energetic diagnostics include those of *Pinardi and Robinson* [1987], who diagnosed jet and cyclone formation in the thermocline, *Robinson et al.* [1988], who applied this procedure to Gulf Stream ring formation, and *Masina and Pinardi* [1993], who discussed energetics of eddy merger (or nonmerger) in QG flows. Additionally, M95 diagnosed a cold tongue intrusion of the Iceland-Faroe

frontal current to be a relatively clear-cut case of baroclinic instability; the east-west oriented shear flow of the IFF rapidly developed a wavelike structure through thermocline energetic transfers from gravitational to kinetic energy and subsequent transfers of energy upward through the water column.

In the present situation, the initial geometry of the frontal current is much more complicated compared with the east-west current encountered initially by M95. Furthermore, the energy exchange patterns seen in the benchmark cases of Pinardi and Robinson are for fixed "mean" flows and small-amplitude wavelike solutions. In our simulations of frontal current variability, the flow is fully nonlinear with no well-defined background mean flow or simple wavelike perturbation. Also the variations in energy exchange processes are neither stationary in time nor fixed in space, so that areal averages of the balances are moot. Nonetheless, it turns out to be relatively straightforward to identify key features of the variations in energy that are indicative of a strongly baroclinically unstable current field, as discussed subsequently.

### 8.1. The Southeastward Shift

The initial steplike shape of the frontal current on August 15 is smoothed out and permuted to a southeastward flowing current by the presence of baroclinic wavelike disturbance in the middle three layers of the model. As the disturbance propagates southeastward, it yields a net conversion of gravitational energy into kinetic via the buoyancy coupling term. Plate 2 shows a time sequence (days 1–3) of the layer 3 (250-m) stream function (column 1) along with the plots of the three central terms in the conversion process (columns 2–4). The source term for baroclinic instability is the horizontal advective working rate on the AGE (Plate 2, column 2) and is the key effect discernible in the middle water column. It has a wave-packet structure centered on the kink in the initial current and leads the southeastward progressing frontal current. It has a predominantly positive sign (indicating forcing of the AGE) and also has the same shape (but opposite sign) as the buoyancy-coupling term, which transfers energy to the KE equation.

In the KE budget, the vertical pressure flux divergence term has an opposite sign to the buoyancy term in layer 3 with the net effect of exporting KE upward to level 2. At level 2 (150-m), baroclinic conversion (i.e., conversion of AGE to KE via the buoyancy coupling term) is also active, so that the vertical pressure flux divergence is partly being driven from level 3 (same sign as buoyancy coupling) and

**Table 4.** Forecast Skill Versus Persistence of Day Zero: QG Forecast for August 21–23

| | Dynamic Height in Layers 1, 2, and 3 | | | |
|---|---|---|---|---|
| | Region 2 | | Region 4 | |
| | ACC Change | rmse Change, % | ACC Change | rmse Change, % |
| Case 3 | — | — | +0.322 | +4 |
| | — | — | +0.292 | +14 |
| | — | — | +0.297 | +47 |
| Case 4 | +0.083 | −11 | +0.261 | −8 |
| | +0.062 | −9 | +0.239 | −5 |
| | +0.049 | +4 | +0.230 | +9 |

## PSI-1 DAY-0/TRAX AUG-18

## PSI-1 DAY-1/TRAX AUG-19

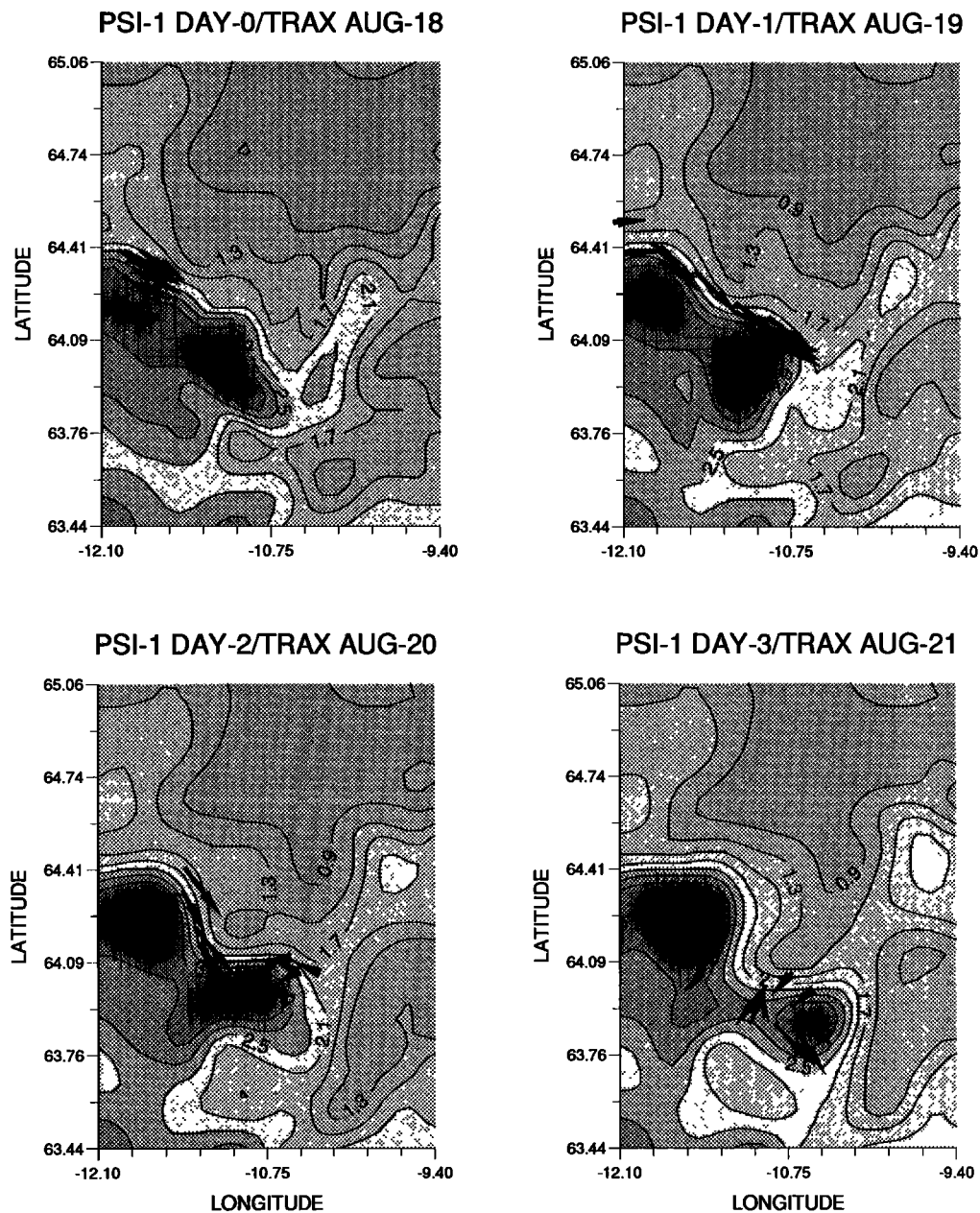## PSI-1 DAY-2/TRAX AUG-20

## PSI-1 DAY-3/TRAX AUG-21

**Figure 12.** Case 3 initial condition (August 18) and day 1 through day 3 forecasts (August 19–21) of 50-m nondimensional stream function (CI = 0.4; multiply by 4500 to redimensionalize to $m^2/s$). Observed 12-hour drifter displacements for each day are plotted as arrows.

partly driven from the buoyancy coupling at level 2 (opposite sign of buoyancy). Since buoyancy coupling is not active near the surface (layer 1 at 50 m), the dominant forcing effect is from the vertical pressure flux divergence, and the horizontal pressure work force is the main balancing term. The source term for barotropic instability is the advective working rate on the KE, but it is very weak compared with the magnitude of the pressure work terms. This indicates the overwhelming dominance of baroclinic instability processes during this time interval.

### 8.2. The Hammerhead Intrusion

From the initially southward oriented frontal current on August 18, the cold intrusion in case 3 arises dynamically as

follows. Plate 3 shows the time sequence of the important baroclinic conversion terms for this case. Initially, a baroclinic disturbance centered on the southeastern extremity of the frontal current draws energy from the AGE via the advective working rate term in a similar fashion as described for case 1 (for indeed, it is a continuation of the baroclinic wave evolution of case 1). Transformation by buoyancy coupling to the KE equation at middepth as well as upward transfer of energy via vertical pressure work occurs in this case also. The wavelike disturbance causing baroclinic conversion migrates southeastward, resulting in the strengthening of the eastward current along the southern face of the hammerhead intrusion and strengthening of the southward flow in the southeastern subdomain.
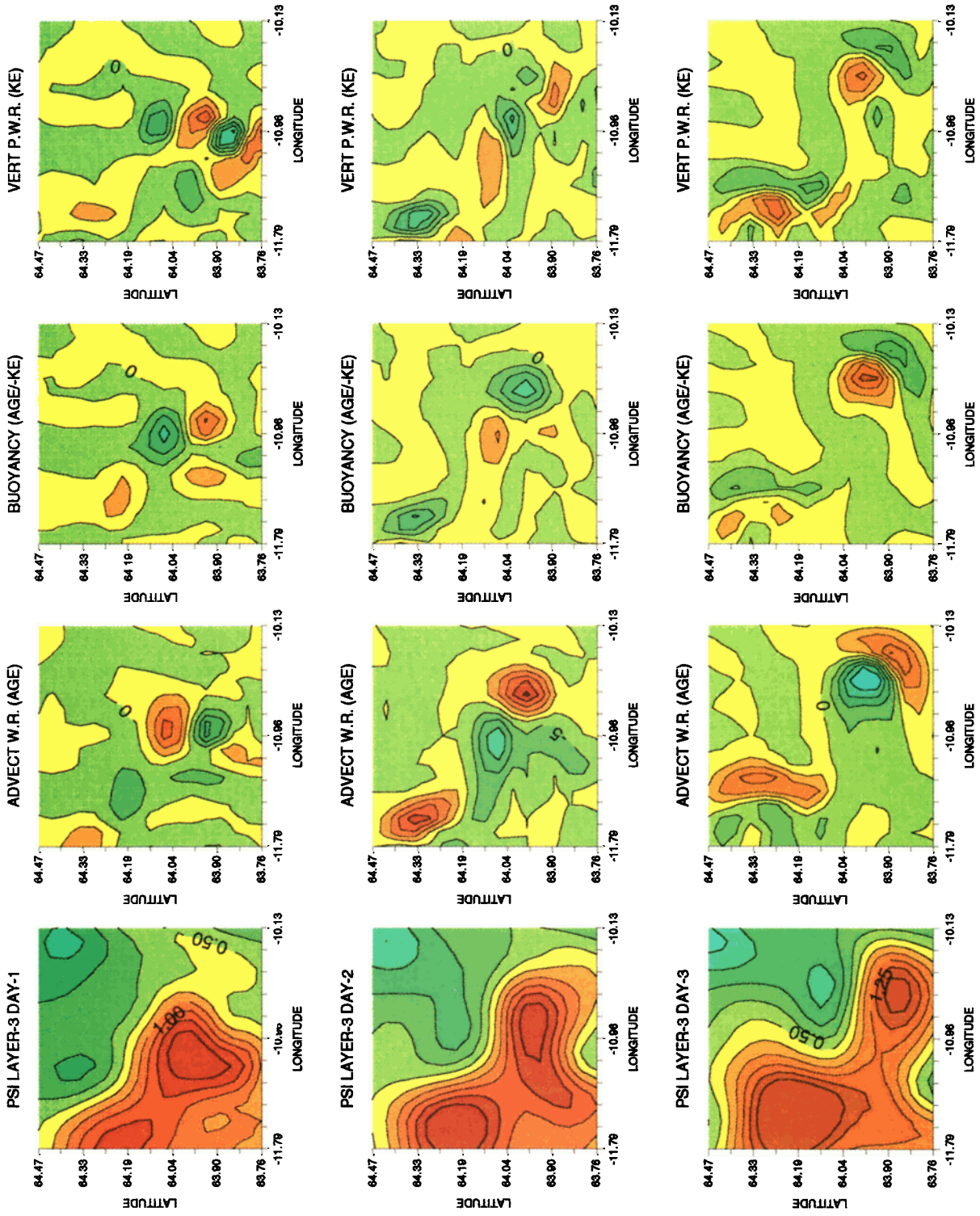
Plate 3. As in Plate 2 but for case 3 in subdomain displaced one grid point north and west of that in Plate 2.

Apparently independently of that baroclinic disturbance, another disturbance grows in the northwestern part of the subdomain, drawing energy from the AGE and strengthening the eastward flowing frontal current from August 19 to 21. At that point the basic structure of the cold hammerhead intrusion arises in the dynamic height field, namely, strong eastward flow from the inflow at 64.4°N, southwestward flow along the western flanks of the cold intrusion, and strong eastward flow along the base of the hammerhead. It is remarkable that the hammerhead intrusion develops as a result of an extension of the eastward flowing inflow current rather than as a localized perturbation on a preexisting east-west frontal current. This result suggests that large-scale current fields external to the observational and modeling region serve to set up the inflow jet boundary conditions, which then aid in controlling the subsequent variations of baroclinically unstable Iceland-Faroe frontal current.

Thus very similar baroclinic conversion processes and upward transfer of energy from the middepths to the surface, occur in both case 1 and case 3, as well as in M95. The process is manifested through the occurrence of baroclinic wavelike disturbances, which lead the strengthening current field and have a localized net effect much like the wave perturbations that are solutions of infinite geometry or semi-infinite geometry linearized baroclinic instability problems. These results therefore show that the rapidly changing meanders of the Iceland-Faroe frontal current are controlled by baroclinically unstable waves that grow and interact with the evolving current field. The potential importance of baroclinic instability in the IFF has previously been identified in the studies by *Willebrand and Meincke* [1980] and *Allen et al.* [1994].

## 9. Summary and Discussion

We have shown evidence for quantitative skill in quasi-geostrophic forecasts of Iceland-Faroe frontal variability for two different initial conditions, executed in real time (or near real time) while onboard ship. The first forecast indicated a shift in direction of frontal current flow, and the skill scores revealed the anomaly correlation coefficient increased 0.07–0.11 relative to persistence of day zero, plus slight reduction of the rms error. The second forecast was far superior to persistence of day zero, as quantified by the correlation statistic (increases exceeding 0.20) and modeled the rapid growth of a cold hammerhead intrusion (or "deep-sock meander") along the frontal current boundary.

The growth of the cold hammerhead intrusion did not occur locally along an east-west oriented frontal current, as had the cold tongue intrusion investigated by *Miller et al.* [1995]. It was rather created as a result of an extension of the inflow current from the western boundary of the domain. Since the model is forced solely by the persistent boundary inflow conditions, this aspect of the simulation suggests that a large-scale current field external to the sampling domain strongly aids in controlling the intense variations of the frontal current.

Using energetic diagnostics, we investigated the physical mechanisms that controlled variations in the current structure along the front. The fundamental mechanism for variability of the Iceland-Faroe frontal current, commencing from both initial states, was clearly baroclinic instability, whereby baroclinic wavelike disturbances grew along the

frontal current, with the net effect of draining energy from the vertical shear flow and transferring it to kinetic energy. The fully nonlinear modeled flows from the two initial states are remarkably similar behaviorally, in the sense that growth of localized baroclinic disturbances occurred in both cases (and in two different places at the same time for the second initial state).

This presentation of quantitative skill in open-ocean forecasts of mesoscale variability is particularly noteworthy because it is the first time nearly complete initialization and validation data sets have been available and specifically applied to real-time shipboard forecasts. Yet since only two initial states were available, we are unable to attach significant statistical confidence to the impressive skill scores of the forecasts. Furthermore, since the boundary conditions are held fixed during the forecasts, one cannot expect QG forecasts of the Iceland-Faroe frontal current to be skillful much longer than the 3- to 4-day timescale found here, since information migrating from the horizontal and vertical boundaries will eventually corrupt the predictions in the interior region. Nonetheless, as shown in our previous work [*Miller et al.*, 1995], the QG dynamics are plausible and dynamically consistent with previous diagnostic studies. These new results further substantiate the validity and utility of the QG model forecasting the rapid evolution of the Iceland-Faroe frontal current and suggest that even better results can be anticipated with primitive equation forecasting models.

## References

Allen, J. T., D. A. Smeed, and A. L. Chadwick, Eddies and mixing at the Iceland-Faroes Front, *Deep Sea Res., Part I, 41*, 51–79, 1994.

Carter, E. F., and A. R. Robinson, Analysis models for the estimation of oceanic fields, *J. Atmos. Oceanic Technol., 4*, 49–74, 1987.

Ezer, T., D.-S. Ko, and G. L. Mellor, Modeling and forecasting the Gulf Stream, *Mar. Technol. Soc. J., 26*, 5–14, 1992.

Fox, D. N., M. R. Carnes, and J. L. Mitchell, Characterizing major frontal systems: A nowcast/forecast system for the northwest Atlantic, *Oceanography, 5*, 49–54, 1992.

Fox, D. N., M. R. Carnes, and J. L. Mitchell, Circulation model experiments of the Gulf Stream using satellite-derived fields, *Formal Rep. 9412*, 46 pp., Nav. Res. Lab., Stennis Space Cent., Miss., 1993.

Glenn, S. M., and A. R. Robinson, Validation of a Gulf Stream forecast model, in *Quantitative Skill Assessment for Coastal Ocean Models, Coastal Estuarine Ser.*, vol. 47, edited by D. R. Lynch and A. M. Davis, AGU, Washington, D. C., pp. 469–487, 1995.

Holloway, G., and B. J. West (Eds.), *Predictability of Fluid Motions*, 612 pp., American Institute of Physics, New York, 1984.

Masina, S., and N. Pinardi, The halting effect of baroclinicity in vortex merging, *J. Phys. Oceanogr., 23*, 1618–1637, 1993.

Miller, A. J., H. G. Arango, A. R. Robinson, W. G. Leslie, P.-M. Poulain, and A. Warn-Varnas, Quasi-geostrophic forecasting and

physical processes of Iceland-Faroe Front variability, *J. Phys. Oceanogr.*, in press, 1995.

Miller, R. N., A. R. Robinson, and D. Haidvogel, A baroclinic quasigeostrophic open ocean model, *J. Comput. Phys.*, *50*, 38–70, 1981.

Niiler, P. P., S. Piacsek, L. Neuberg, and A. Warn-Varnas, Sea surface temperature variability of the Iceland-Faeroes Front, *J. Geophys. Res.*, *97*, 17,777–17,785, 1992.

Pinardi, N., and A. R. Robinson, Quasigeostrophic energetics of open ocean regions, *Dyn. Atmos. Oceans*, *10*, 185–219, 1986.

Pinardi, N., and A. R. Robinson, Dynamics of deep thermocline jets in the POLYMODE region, *J. Phys. Oceanogr.*, *17*, 1163–1188, 1987.

Poulain, P.-M., Cruise report for R/V *Alliance* cruise: GIN93, Wilhelmshaven-Bodo, 11–26 August, 1993, SACLANT Undersea Res. Cent., La Spezia, Italy, 1993.

Robinson, A. R., and L. J. Walstad, The Harvard Open Ocean Model: Calibration and application to dynamical process, forecasting, and data assimilation studies, *Appl. Numer. Math.*, *3*, 89–131, 1987.

Robinson, A. R., M. A. Spall, and N. Pinardi, Gulf Stream simulations and the dynamics of ring and meander processes, *J. Phys. Oceanogr.*, *18*, 1811–1853, 1988.

Robinson, A. R., S. M. Glenn, M. A. Spall, L. J. Walstad, G. M. Gardner, and W. G. Leslie, Forecasting Gulf Stream meanders and rings, *Eos Trans. AGU*, *70*, 1464–1465, 1473, 1989.

Willebrand, J., and J. Meincke, Statistical analysis of fluctuations in the Iceland-Scotland frontal zone, *Deep Sea Res., Part A*, *27*, 1047–1066, 1980.

H. G. Arango, W. G. Leslie, and A. R. Robinson, Division of Applied Sciences and Department of Earth and Planetary Sciences, Harvard University, Cambridge, MA 02138.

A. J. Miller, Climate Research Division, Scripps Institution of Oceanography, La Jolla, CA 92093-0224.

P.-M. Poulain and A. Warn-Varnas, SACLANT Undersea Research Centre, 19138 La Spezia, Italy.